Generation of control signals using second-Nyquist zone technique for superconducting qubit devices

Ujjawal Singhal,[1, *] Shantharam Kalipatnapu,[2, *]

Sourav Majumder,[1] Vaibhav Venkata Lakshmi Pabbisetty,[2]

Srivatsava Jandhyala,[2] Vibhor Singh,[1, †] and Chetan Singh Thakur[2, ‡]

[1]*Department of Physics, Indian Institute of Science, Bangalore-560012 (India)*

[2]*Department of Electronic Systems Engineering,*

Indian Institute of Science, Bangalore-560012 (India)

(Dated: March 4, 2022)

Abstract

There is growing interest in developing integrated room temperature control electronics for the control and measurement of superconducting devices for quantum computing applications. With the availability of faster DACs, it has become possible to generate microwave signals with amplitude and phase controls directly without requiring any analog mixer. In this report, we use the evaluation kit ZCU111 to generate vector microwave pulses using the second-Nyquist zone technique. We characterize the performance of the signal generation and measure amplitude variation across second Nyquist zone, single-sideband phase noise, and spurious-free dynamic range. We further perform various time-domain measurements to characterize a superconducting transmon qubit and benchmark our results against traditionally used analog mixer setups.

Keywords: control-electronics, FPGA, superconducting qubit, quantum computing

---

* These two authors contributed equally

† Correspondence email address: v.singh@iisc.ac.in

‡ Correspondence email address: csthakur@iisc.ac.in

I. INTRODUCTION

Quantum processors utilize the properties of quantum parallelism and quantum interference in solving certain computational problems much faster than classical computers [1]. Qubits which are the building blocks of quantum processors have many realizations such as trapped ions [2], semiconducting quantum dots [3], nitrogen-vacancy centers [4], and superconducting qubits [5, 6] etc. Among several such realizations, superconducting qubits are being aggressively pursued for scalable quantum computing platform [7, 8]. The superconducting qubits are essentially nonlinear oscillators, which utilize the nonlinearity of the Josephson inductance to form an effective quantum two-level system [9]. These systems need microwave pulses with gigahertz (GHz) frequency and latency in nanoseconds for control and readout, which are realized by the high speed electronics at room temperature [6, 10, 11].

Traditionally for superconducting qubits, commercially available arbitrary waveform generators (AWG) based on Radio Frequency-Digital to Analog Converters (RF-DAC) with ¡ 1 GHz of analog bandwidth have been used. These are usually designed for general purpose tests and measurements. RF qubit control pulses, which are typically 4-6 GHz are obtained by upconverting the AWG waveforms with analog mixers. These analog mixers come with a Local Oscillator (LO) leakage and imperfect sideband suppression [12], and their electrical properties vary with manufacturing tolerance and environmental effects. This demands a periodic calibration of the mixers to suppress unwanted image frequencies which is an overhead to the experiments [12]. This invites the need for a customized engineering solution that meets the requirement of the quantum computing community. Integration of FPGA with RF-DAC and ADC have led to several breakthroughs such as active-reset, pulse-routing [13], faster readout [14], stabilization of Rabi-oscillations [15], quantum error correction [16, 17]. These hardware implementations have reached sufficient maturity and several commercial products from different vendors are also available [18–20].

The availability of RF-DACs with high sampling rates in the order of gigahertz frequencies has gained interest in recent times. The Xilinx Zynq Ultrascale+Radio Frequency System-On-Chip (RFSoC) [21] which is a family of devices of Field Programmable Gate Arrays (FPGA) comes with Digital to Analog Converters (DACs) and Analog to Digital Converters (ADCs) of very high sampling rates. It also includes up/down frequency converters using internal digital
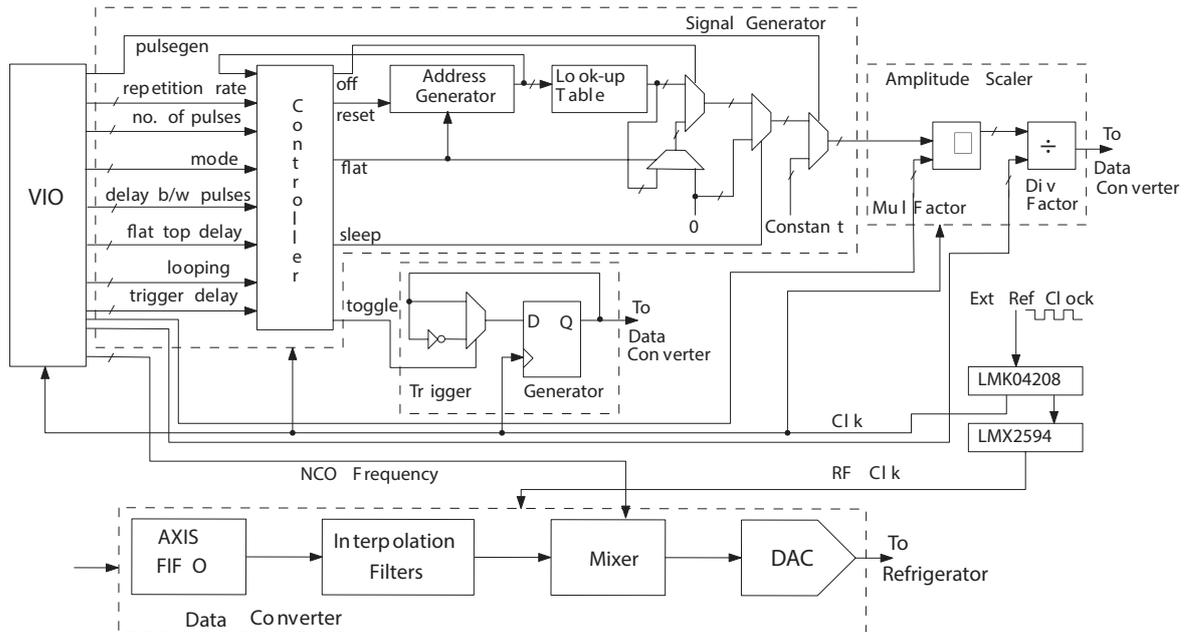
FIG. 1. Block Diagram for the RF Signal Generation

mixers which eliminates the need for external analog mixers. In this work, a single FPGA board (ZCU111 by Xilinx) that is populated with the XCZU28DR device has been used to directly generate control pulses in 4-5 GHz frequency range using the Second-Nyquist zone techniques. Our method therefore, eliminates the requirement of any analog mixer. We first benchmark the performance of the Continuous Wave (CW) microwave signals at room temperature by measuring various parameters like spurious-free dynamic range (SFDR), single-sideband phase noise and the reduction in amplitudes while generating signals in multiple Nyquist zones. To show the applicability of our technique, we generate the control pulses required for the control of the superconducting qubit and carry out coherence measurements of a transmon qubit.

II. RF PERFORMANCE BENCHMARKING

A. FPGA Logic for the Generation of RF Control Signals and Waveforms

This section describes the design for arbitrary waveform generation through DAC in higher Nyquist zones. It further describes the experiments conducted to benchmark the performance

of the continuous microwave signals through ZCU111. We use the first generation of RFSoC device XCZU28DR for our experiments. It comes with eight high precision and low power DACs and ADCs with maximum sampling rates of 6.554 GSPS and 4.096 GSPS, respectively. These data converters are configurable and integrated with Programmable Logic (PL) resources of the RFSoC through AXI interfaces. The eight DACs are clocked by primary onboard reference Phase Locked Loop (PLL) LMK04208 and onboard RF PLL LMX2594 to generate the sample clocks [22] of the data converters. On the ZCU111 evaluation board, two DACs and two ADCs routed to HF baluns with –1dB Pi pad attenuators, two DACs, and two ADCs routed to LF baluns with -3dB Pi pad attenuators, and remaining four DACs, and four ADCs routed to SMAs for use with external custom baluns and filters, all being routed to SMAs [22]. The baluns are primarily added to attenuate higher image frequency signals generated by DAC.

Figure 1 shows the stages involved in generating the RF control signals. The *Signal Generator Block* produces continuous and shaped pulse waveforms required as per the measurement experiment. The sample values of the function are stored in a look-up table whose address is provided by the *Address Generator Block*. The *Controller Block* provides the necessary control signals based on the input parameters, which enables the *Signal Generator Block* to produce the appropriate waveform.

The *Amplitue Scaler Block* in Figure 1 scales the amplitude of generated samples appropriately on the fly. The amplitude scaling is realized by the multiplier and the divider units. The RF-DAC is a 14-bit signed DAC with a 16-bit digital signal processing path, resulting in a amplitude resolution of $\frac{V_{FS}}{2^{13}}$, where V_{FS} is the full-scale voltage. An external 10 MHz clock is fed to LMK04208 to synchronize the timebase of the FPGA board with other instruments. The *Data Converter Block* consists of a First In First Out (FIFO), an interpolation filter, a mixer, and a DAC as shown in Figure 1. The scaled sample values from the *Amplitude Scaler Block* are fed into AXI Stream (AXIS) FIFO of the corresponding DAC channel. At higher Sampling rates of Data Converters, the data streaming clock of the DAC cannot be pushed in the orders of their sampling rates. So a digital upsampling is necessary. This function on the DAC side is realized by the Interpolation Filters. The interpolation rate can be chosen among 1x, 2x, 4x, and 8x. A 48-bit *Numerically Controlled Oscillator* (NCO) is included with the IQ-mixer, which is used to upconvert the baseband signal to an RF range whose frequency can be changed on the fly. This 48-bit is a signed integer representation of frequencies in the range from $\frac{-F_S}{2}$ to $\frac{F_S}{2}$, resulting in

a frequency resolution of $\frac{F_S}{2(2^{47}-1)}$, where F_S is the sampling rate of Data Converter. We encode the frequencies in the range $\frac{-F_S}{2}$ to $\frac{F_S}{2}$ and to generate a frequency above $\frac{F_S}{2}$ we find its image frequency in the range 0 to $\frac{F_S}{2}$.

The major advantage of this approach is that RF signal is generated using NCO and a digital IQ-mixer, therefore, it allows a full vector control of amplitude and phase. Since the mixing takes places in digital-domain, such signals are free from local oscillator (LO) leakages as compared to the single-sideband signals generated using analog-IQ mixers requiring periodic calibration. For the time-domain applications, the synchronization between the control signals from the board and qubit-readout setup, a trigger signal is generated through another DAC channel. The delay between the end of the gaussian pulses and the start of the trigger is also configurable. It is important to mention here that ZCU111 comes with 128 numbers of GPIO pins which in principle can be used for synchronization and hand-shaking with other instruments.

For the performance benchmarking and time-domain applications, we require specific parameters of the signals to be changed on the fly. These parameters could be the number of shaped-pulses, their repetition-rate, trigger delay, the delay between two shaped-pulses, frequency of NCO, pulse generation mode, looping, multiplication, and division factors. This is realized by using a Virtual Input Output (VIO), a Xilinx IP, which allows changing the parameters on the fly. The mode bits specified in Figure 1 allow generating pulses that suit different experiments. The pulsegen parameter allows choosing between playing shaped pulses or continuous waveforms. The looping parameter helps to run an experiment in a loop fashion which helps to automate the experiment.

B.   Multi-Nyquist Zone Operation

According to Nyquist criteria, the sampling rate limits the frequency that can be faithfully reconstructed to be less than half the sampling rate. However, in practice, when a signal is sampled, its images appear at higher frequencies. Each Band of the spectrum with width $\frac{F_S}{2}$ is termed as Nyquist Zone (NZ). For example, the range from DC to $\frac{F_S}{2}$ is termed as first-Nyquist Zone, $\frac{F_S}{2}$ to F_S is called second-Nyquist Zone and so on [23]. The images above the first-Nyquist zone can be utilized according to the need. The output voltage of DAC can be represented [24]
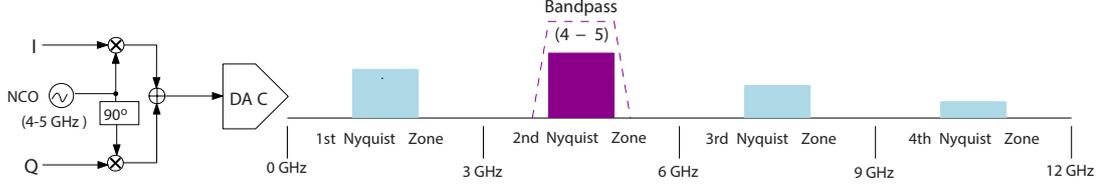
FIG. 2. Upconversion scheme on RFSoC using the on-chip IQ mixer and a numerically controlled oscillator. Using the maximum sampling rate $F_S = 6.554$ GHz, and mode of operation of DAC, the signal/image can be pushed in the second Nyquist zone which can can be conditioned using a Mini-circuit VBFZ-3590-S+(15542) bandpass filter.

as,

$$v\left(t\right) = \left[x\left(t\right) \sum_{k=-\infty}^{\infty} \delta\left(t - kT\right)\right] * r\left(t\right), \qquad (1)$$

where $x\left(t\right)$ is the desired waveform whose samples are being generated, $r(t)$ is the reconstruction waveform, and $T = \frac{1}{F_S}$. Taking Fourier transform on both sides of the above equation, we get

$$V\left(\omega\right) = \left[X\left(\omega\right) * \sum_{n=-\infty}^{\infty} \delta\left(\omega T - 2\pi n\right)\right] R\left(\omega\right), \qquad (2)$$

where $V\left(\omega\right)$, $X\left(\omega\right)$ and $R\left(\omega\right)$ represent the Fourier transform of $v\left(t\right)$, $x\left(t\right)$ and $r\left(t\right)$, respectively. From equation 1 and 2, it becomes evident that the sampled signal is passed through a system having transfer function $R\left(\omega\right)$ and when a signal is sampled we get signal copies in higher frequency ranges. Therefore, the output signal strength of the signal copies in different frequencies range gets affected according to the response of $R\left(\omega\right)$.

The RFSoC supports two modes of operation for DAC: Normal mode or Non-Return-to-Zero (NRZ) mode and Mix mode or Return-to-Complement (RTC) mode which determines $R\left(\omega\right)$. In the NRZ mode of operation the DAC uses a fixed level reconstruction waveform during one clock cycle. It has high output power in the first Nyquist zone, but low output power in the second Nyquist and beyond. RTC mode or the mixed mode, it outputs the sample for the first half of the clock period and then inverts the sample for the second half of the clock period. The resulting frequency response shows high power in the second Nyquist zone and attenuation in the first Nyquist zone. The output power goes to zero at DC, and $2F_S$. This mode provides highest power for the second Nyquist zone applications. Mathematically, the reconstruction waveforms can be

written as,

$$R\left(\omega\right) = \begin{cases} Te^{-i\omega T/2}\operatorname{sinc}\left(\frac{\omega T}{2}\right) & \text{NRZ mode} \\ Tie^{-i\omega T/2}\operatorname{sinc}\left(\frac{\omega T}{4}\right)\sin\left(\frac{\omega T}{4}\right) & \text{RTC mode} \end{cases}$$

The maximum sampling rate of DACs in RFSoC is 6.554 GSPS. Since the frequencies necessary for the control side of qubit are typically in the range of 4-6 GHz, the desired RF band for signal synthesis fall in the second Nyquist zone. It can be accessed by operating in mix mode while maintaining highest power. To suppress the images in other Nyquist zones and signal conditioning, we use standard coaxial bandpass filters. A schematic of the flow and different Nyquist zones are shown in Figure 2.

C. Performance Benchmarking

To measure the power dependency in NRZ and RTC modes, the DAC output response is being characterized by enabling the NCO whose frequency is changed on the fly and the corresponding magnitude is recorded. To compensate for the loss in magnitude, an inverse sinc filter is applied in both modes of operation. The recorded DAC output response is shown in Figure 3(a). The DAC output response in NRZ mode follows a sinc function. It is evident from the Figure 3(a) that the signal power is maximum in the second and third Nyquist zone when operating in the RTC mode. Another important benchmarking metric for continuous mode of operation is the single-sideband phase noise. A frequency tone (carrier) is generated, and at various offset frequencies from the carrier, the power is measured in a specified bandwidth of 1 Hz. We use a signal analyzer (Rohde and Schwartz FSV-13) to perform the phase noise measurements. Figure 3(b) shows the measurement of SSB phase noise plotted for different offset frequencies around the carrier frequency of 4.5 GHz generated from the XCZU28DR device. These are comparable to the phase noise performance of standard test and measurements RF Signal generators [25–28].

While generation of signal using multi-zome Nyquist technique expands the scope of frequency domain capabilities of a DAC, the images generated in other zones need to be carefully suppressed to achieve a practically useful spurious-free dynamic range (SFDR) [29]. Figure 3(c) shows the various spurs for a carrier tone of 4.5 GHz while using a standard bandpass-filter minicircuit VBFZ-3590-S+(15542). With this general purpose filter, we achieve a SFDR of nearly 45 dB.
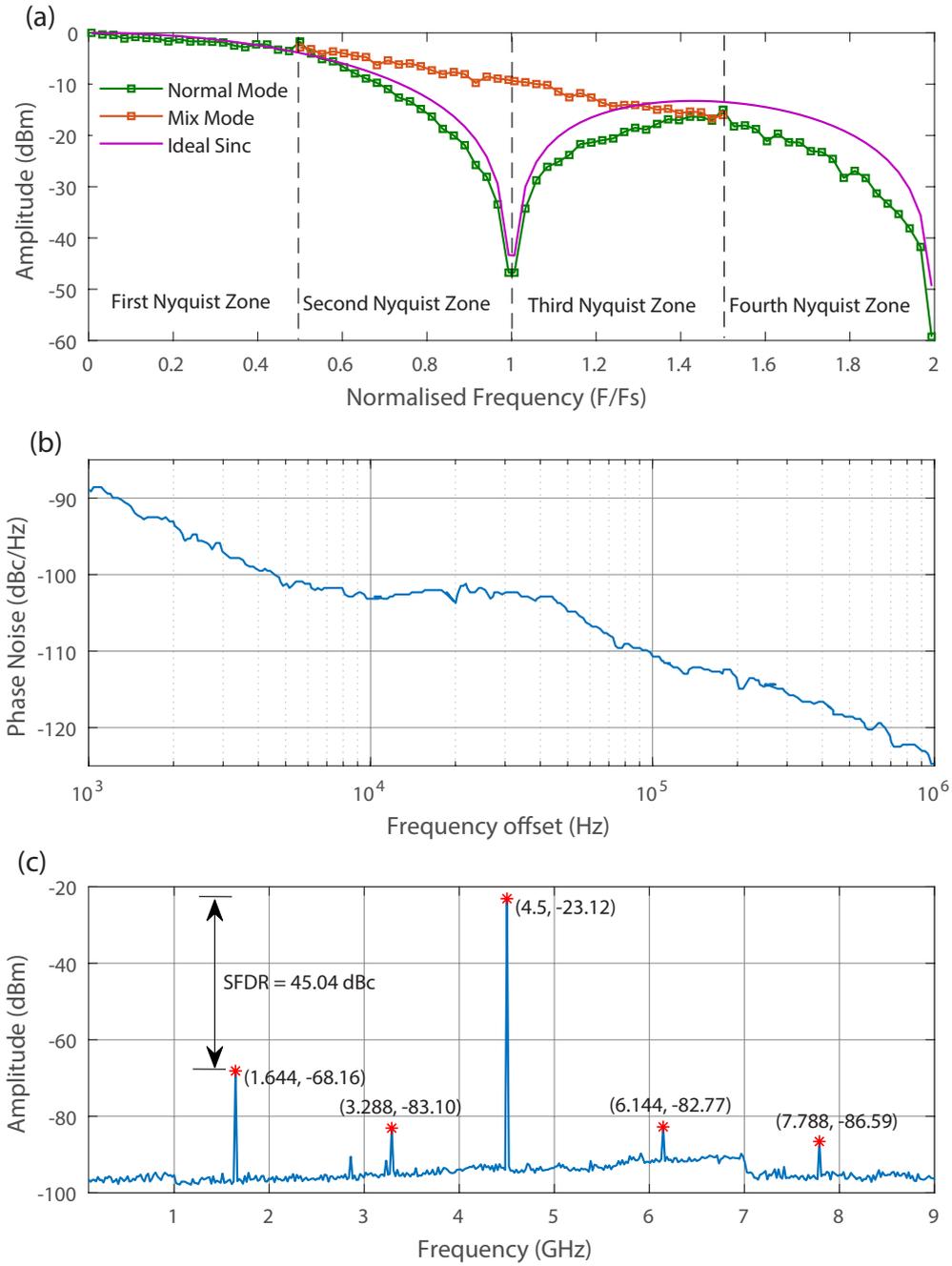
FIG. 3. RF performance evaluation of XCZU28DR: (a) amplitude response of the DAC across various Nyquist zones in normal mode (NRZ) and mix mode (RTC mode). A plot of sinc function in included for comparison. (b) Single sideband (SSB) phase poise of XCZU28DR at carrier frequency of 4.5 GHz. (c) A large span spectrum for the measurement of SFDR at 4.5 GHz carrier tone.

TABLE I. Spurious free dynamic range obtained while operating in the second Nyquist zone in RTC mode and using minicircuits VBFZ-3590-S+(15542) band pass filter for signal conditioning

Frequency (GHz)	SFDR (dBc)
4.1	38.6
4.2	35.4
4.3	39.4
4.4	38.1
4.5	45.0

Our focus in this study has been on the generation of control signals for the superconducting qubits in the frequency range of 4-4.5 GHz. In this range, the SFDR for XCZU28DR device is summarized in Table I. It is important to mention here that this value is currently limited by the choice of the filter, and can be further improved by using tunable cavity or switchable filter banks [30, 31].

III. COHERENCE MEASUREMENTS OF A SUPERCONDUCTING QUBIT

To benchmark the performance of our technique for the direct generation of control signal pulses, we use a superconducting transmon qubit coupled to a 3D waveguide copper cavity. A fixed-frequency transmon qubit was fabricated on an intrinsic silicon wafer using standard lithography processes. The whole qubit-cavity setup was then mounted to the base flange of a dilution refrigerator with various attenuators and filters on the inputs microwave lines. A schematic of the full measurement setup is shown in Fig. 4. By carrying out cavity-qubit spectroscopy, we find the cavity frequency $\omega_c/2\pi = 5.995$ GHz, qubit frequency $\omega_q/2\pi = 4.2$ GHz, cavity linewidth of 1.7 MHz, qubit-cavity coupling $g/2\pi = 44$ MHz, and a qubit anharmonicity of 300 MHz [32].

To demonstrate the applicability of the directly synthesized control pulses, we carry out time-domain coherence measurements of the superconducting qubit. Generally, these experiments are done in two steps. The first step involves amplitude calibration of X_π pulse which corresponds to a 180° rotation of the qubit state about the X-axis. It involves measuring the excited state qubit population while varying the amplitude of the Gaussian pulse resonant with the qubit frequency,
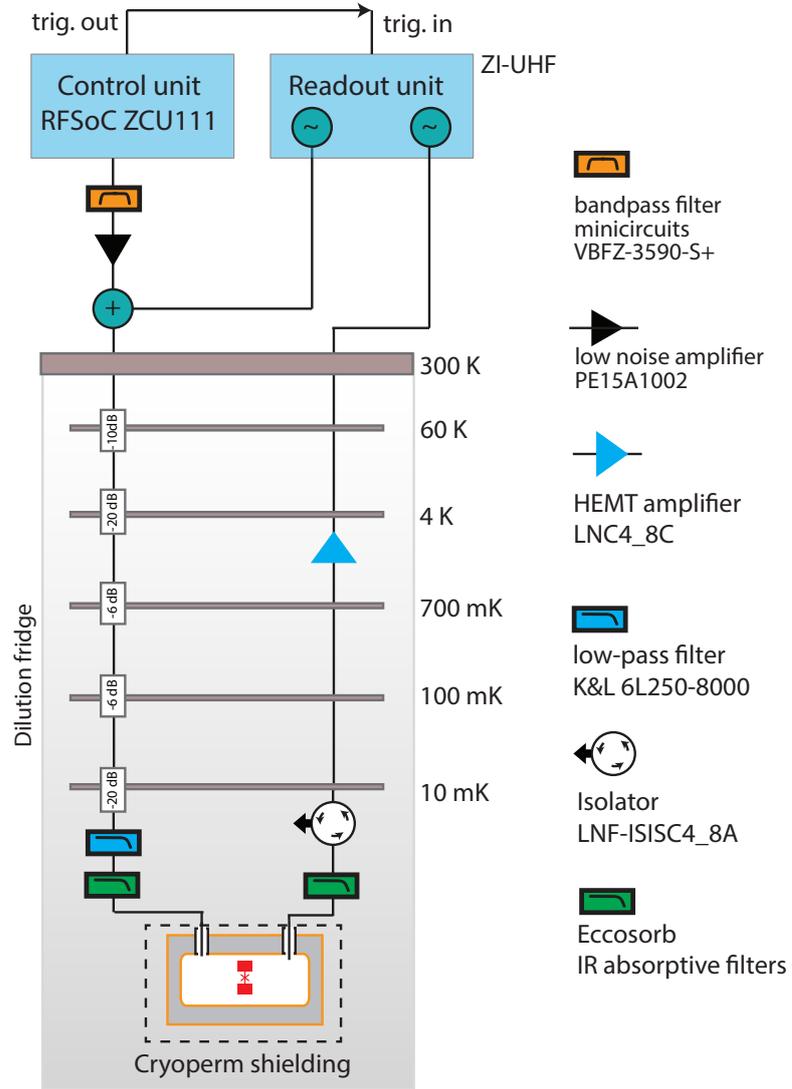
FIG. 4. Experimental measurement setup of superconducting qubit devices : The input lines are used for qubit state manipulation and to send cavity probe signals. First, the control signal was boosted up by using a Pasternack low noise amplifier, and then it was added together with the readout signal. Both the signals then traveled to the device through the series of attenuators, tubular low pass filter, and homemade IR filter. The output signal from the cavity is then amplified by a HEMT amplifier mounted on the 4K stage and then the cavity quadratures were measured directly using the ZI-UHF lock-in amplifier.

a measurement colloquially known as power-Rabi measurement. For these measurements, we use 260 ns long Gaussian pulses with a standard deviation of 65 ns. As the qubit frequency and hence the control signal frequency falls in the second-Nyquist zone, we use a wide-band Pasternack (PE 15A1002) amplifier to boost the signal amplitude to overcome the attenuation.

We use the UHF-AWG from Zurich Instruments to determine the in-phase and quadrature components of the readout pulse and the subsequent qubit state determination. It is important to mention here that in principle, the fast ADC channels available on ZCU111 can be used for qubit readout and the entire control and readout part can be done on the same board. To address the issue the cross-platform triggering, we generate a trigger from ZCU111 analog output channel and used it to arm the sequencer on UHF-AWG. This straight-forward handshaking allows us to correct any trigger latency by advancing the trigger generation on ZCU111. Moreover, it allows defining simple "loops" on ZCU111 so that the entire experiment can be controlled from the board.

To check the coherent oscillation between the qubit ground state and the first excited state, we carry out Rabi oscillation measurement in time domain. The implement this by inserting a rectangular pulse with variable number of samples, at the center of the X_π gaussian pulse. The duration of qubit control pulse can be adjusted by adjusting the number of sample points in the rectangular pulse. The top part of Fig. 5(a) panel shows the pulse sequence. Any trigger latency between ZCU11 and the readout setup (UHF) is adjusted by adjusting the trigger delay. The bottom panel shows the coherent time oscillations as the duration of control pulse is increased.

After carrying out this measurement, it is straightforward to carry out energy relaxation rate measurement. The setup is same as the Rabi oscillation measurement setup with a minor change in the pulse sequence. Here we first send a calibrated X_π pulse and then wait for time t, before performing a readout as shown in Fig. 5(b). Due to on-the-fly configuration of the delay time, the entire measurement can be controlled by ZCU111 unit. For a given wait time, we generate 50,000 X_π pulses at a repetition rate of 5 kHz and determine the excited state population. Fig. 5(b) shows the results from T_1 measurements. The results from the T_1 experiment along with the fit, yielding a $T_1 = 30.5$ μs.

Next, we carry out the Ramsey experiment, a measurement of dephasing rate. The protocol requires the generation of two $X_{\pi/2}$ pulses with a variable time-delay between them, and subsequently the qubit measurement. A schematic of the pulse sequence and result from the Ramsey
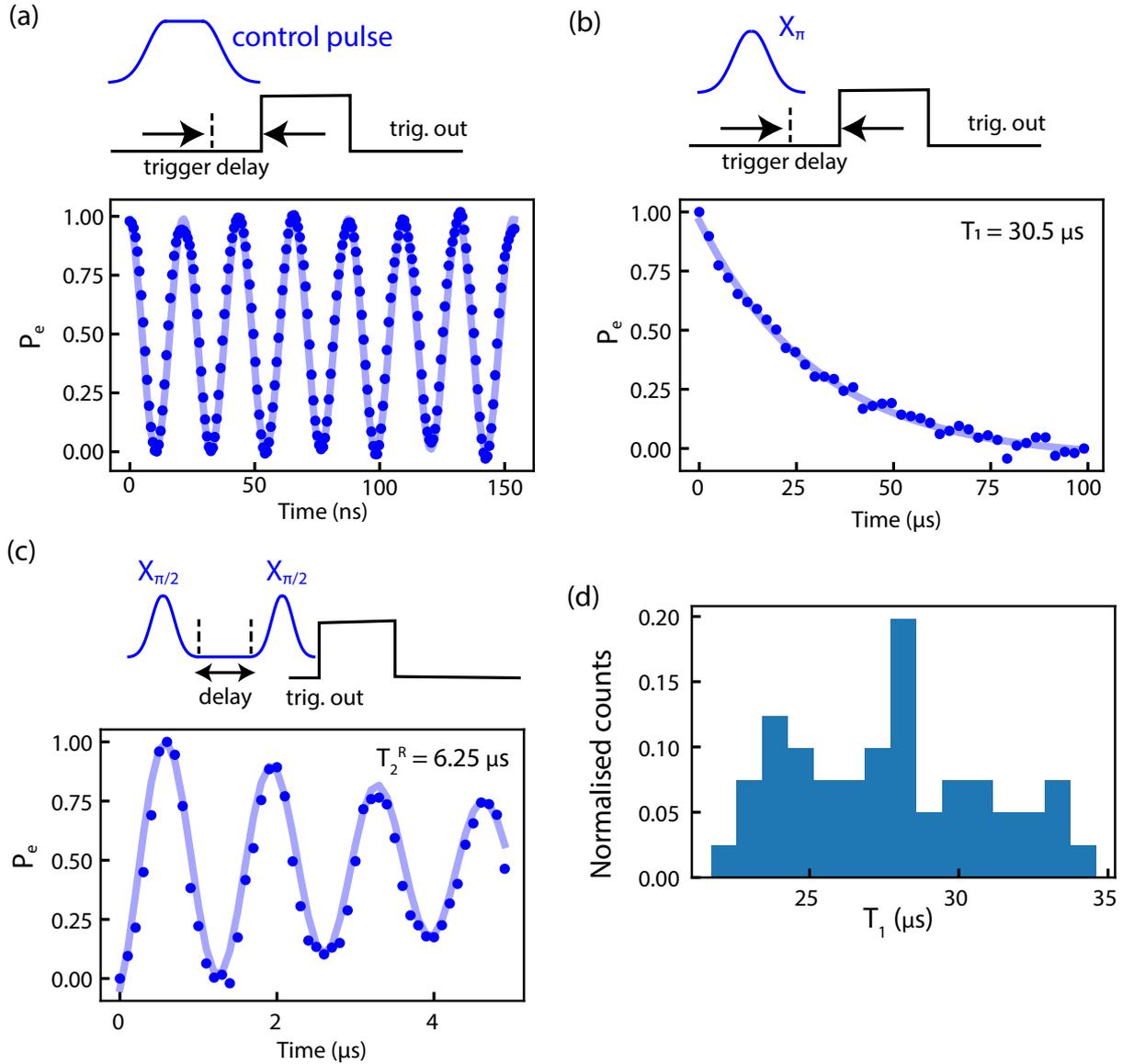
FIG. 5. Time-domain control of a transmon qubit using ZCU111. (a) Rabi oscillations between the qubit's ground $|0\rangle$ and first excited state $|1\rangle$ as a the duration of control pulse is varied. (b) Measurement of the energy relaxation time T_1. The blue line indicates an exponential fit yielding $T_1 = 30.5$ μs. (c) Measurement of Ramsey dephasing time (T_2^R). The top part of the panel shows the pulse sequence. From the fit indicated by solid line, we extract Ramsey dephasing time $T_2^R = 6.25$ μs. (d) Histogram showing the statistical variation between 47 T_1 measurements taken over a period of 24 hours.

fringe experiment is shown in Fig. 5(c). As the experiment can be completely controlled by the ZCU111, the procedure remains similar to the T_1 measurements. Here the trigger for readout unit is aligned to the end of the second $X_{\pi/2}$ pulse and a delay between the two $X_{pi/2}$ pulses is varied. The results from the Ramsey fringe experiment along with the fit, yield a $T_2^R \approx 6.3$ μs. It is important to point out here that since both the $X_{\pi/2}$ pulses are generated by the internal digital IQ-mixer and common NCO, a well-defined phase relation hold between the two pulses. In addition, we would like to emphasize here that the measurements of T_1 and T_2^R on the same device during the same run were also carried out using the conventional single-sideband modulation scheme using a vector source and an arbitrary waveform generator. We do not find any statistically significant difference from the results obtained using ZCU111. Given the ease of the measurements as no periodic calibration for sideband suppression necessary, we also repeated the T_1 measurements over a period of 24 hours and record statistical variations in the T_1 measurements. Fig. 5(d) shows a histogram of 47 T_1 measurements from the same device.

IV. CONCLUSION

To summarize, we demonstrated the generation of microwave signals using the second-Nyquist zone technique on ZCU111. Using the standard off-the-selves components, we show that the performance of signal generation is close to the various commercially available vector sources. We emphasize that SFDR performance can be further improved by using a dedicated set of filter banks rather than the standard test and measurement component used in this work. Looking ahead, we would like to expand the number of control channels and explore the synchronization between different pairs of DACs for two-qubit gates. The capabilities of the ADCs have not been explored in this work and it would be a part of future exploration. With a push of open-source python-based interfacing by research communities, and the continuous improvements in the performance and scaling of RFSoC platform, the control, and measurements of multi-qubit processors can be foreseen to become compact, easy to synchronize, and cost-effective.

V. ACKNOWLEDGMENT

[1] T. D. Ladd, F. Jelezko, R. Laflamme, Y. Nakamura, C. Monroe, and J. L. O'Brien, "Quantum computers," *Nature*, vol. 464, no. 7285, pp. 45–53, Mar. 2010. [Online]. Available: http://www.nature.com/articles/nature08812

[2] S.-L. Zhu, C. Monroe, and L.-M. Duan, "Trapped Ion Quantum Computation with Transverse Phonon Modes," *Physical Review Letters*, vol. 97, no. 5, Aug. 2006. [Online]. Available: https://link.aps.org/doi/10.1103/PhysRevLett.97.050505

[3] N. W. Hendrickx, W. I. L. Lawrie, M. Russ, F. van Riggelen, S. L. de Snoo, R. N. Schouten, A. Sammak, G. Scappucci, and M. Veldhorst, "A four-qubit germanium quantum processor," *Nature*, vol. 591, no. 7851, Mar. 2021. [Online]. Available: https://www.nature.com/articles/s41586-021-03332-6

[4] G. D. Fuchs, V. V. Dobrovitski, D. M. Toyli, F. J. Heremans, C. D. Weis, T. Schenkel, and D. D. Awschalom, "Excited-state spin coherence of a single nitrogen–vacancy centre in diamond," *Nature Physics*, vol. 6, no. 9, Sep. 2010. [Online]. Available: https://www.nature.com/articles/nphys1716

[5] M. H. Devoret and R. J. Schoelkopf, "Superconducting Circuits for Quantum Information: An Outlook," *Science*, vol. 339, no. 6124, pp. 1169–1174, Mar. 2013. [Online]. Available: https://www.science.org/doi/10.1126/science.1231930

[6] M. Kjaergaard, M. E. Schwartz, J. Braumüller, P. Krantz, J. I.-J. Wang, S. Gustavsson, and W. D. Oliver, "Superconducting qubits: Current state of play," vol. 11, no. 1, pp. 369–395. [Online]. Available: https://doi.org/10.1146/annurev-conmatphys-031119-050605

[7] F. Arute, K. Arya, R. Babbush, D. Bacon, J. C. Bardin, R. Barends, R. Biswas, S. Boixo, F. G. S. L. Brandao, D. A. Buell, B. Burkett, Y. Chen, Z. Chen, B. Chiaro, R. Collins, W. Courtney, A. Dunsworth, E. Farhi, B. Foxen, A. Fowler, C. Gidney, M. Giustina, R. Graff, K. Guerin, S. Habegger, M. P. Harrigan, M. J. Hartmann, A. Ho, M. Hoffmann, T. Huang, T. S. Humble, S. V. Isakov, E. Jeffrey, Z. Jiang, D. Kafri, K. Kechedzhi, J. Kelly, P. V. Klimov, S. Knysh, A. Korotkov, F. Kostritsa, D. Landhuis, M. Lindmark, E. Lucero, D. Lyakh, S. Mandrà, J. R. McClean, M. McEwen, A. Megrant, X. Mi, K. Michielsen, M. Mohseni, J. Mutus, O. Naaman, M. Neeley, C. Neill, M. Y. Niu, E. Ostby, A. Petukhov, J. C. Platt, C. Quintana, E. G. Rieffel, P. Roushan, N. C. Rubin, D. Sank, K. J. Satzinger, V. Smelyanskiy,

K. J. Sung, M. D. Trevithick, A. Vainsencher, B. Villalonga, T. White, Z. J. Yao, P. Yeh, A. Zalcman, H. Neven, and J. M. Martinis, "Quantum supremacy using a programmable superconducting processor," *Nature*, vol. 574, no. 7779, pp. 505–510, Oct. 2019. [Online]. Available: http://www.nature.com/articles/s41586-019-1666-5

[8] M. Gong, S. Wang, C. Zha, M.-C. Chen, H.-L. Huang, Y. Wu, Q. Zhu, Y. Zhao, S. Li, S. Guo, H. Qian, Y. Ye, F. Chen, C. Ying, J. Yu, D. Fan, D. Wu, H. Su, H. Deng, H. Rong, K. Zhang, S. Cao, J. Lin, Y. Xu, L. Sun, C. Guo, N. Li, F. Liang, V. M. Bastidas, K. Nemoto, W. J. Munro, Y.-H. Huo, C.-Y. Lu, C.-Z. Peng, X. Zhu, and J.-W. Pan, "Quantum walks on a programmable two-dimensional 62-qubit superconducting processor," *Science*, May 2021, publisher: American Association for the Advancement of Science. [Online]. Available: https://www.science.org/doi/abs/10.1126/science.abg7812

[9] J. Koch, T. M. Yu, J. Gambetta, A. A. Houck, D. I. Schuster, J. Majer, A. Blais, M. H. Devoret, S. M. Girvin, and R. J. Schoelkopf, "Charge-insensitive qubit design derived from the Cooper pair box," *Physical Review A*, vol. 76, no. 4, p. 042319, Oct. 2007. [Online]. Available: http://link.aps.org/doi/10.1103/PhysRevA.76.042319

[10] P. Krantz, M. Kjaergaard, F. Yan, T. P. Orlando, S. Gustavsson, and W. D. Oliver, "A quantum engineer's guide to superconducting qubits," *Applied Physics Reviews*, vol. 6, no. 2, p. 021318, Jun. 2019, publisher: AIP Publishing LLCAIP Publishing. [Online]. Available: https://aip.scitation.org/doi/abs/10.1063/1.5089550

[11] L. B. Nguyen, G. Koolstra, Y. Kim, A. Morvan, T. Chistolini, S. Singh, K. N. Nesterov, C. Jünger, L. Chen, Z. Pedramrazi, B. K. Mitchell, J. M. Kreikebaum, S. Puri, D. I. Santiago, and I. Siddiqi, "Scalable High-Performance Fluxonium Quantum Processor," *arXiv:2201.09374 [cond-mat, physics:quant-ph]*, Jan. 2022, arXiv: 2201.09374. [Online]. Available: http://arxiv.org/abs/2201.09374

[12] S. W. Jolin, R. Borgani, M. O. Tholén, D. Forchheimer, and D. B. Haviland, "Calibration of mixer amplitude and phase imbalance in superconducting circuits," *Review of Scientific Instruments*, vol. 91, no. 12, Dec. 2020. [Online]. Available: https://aip.scitation.org/doi/10.1063/5.0025836

[13] S. Asaad, C. Dickel, N. K. Langford, S. Poletto, A. Bruno, M. A. Rol, D. Deurloo, and L. DiCarlo, "Independent, extensible control of same-frequency superconducting qubits by selective broadcasting," *npj Quantum Information*, vol. 2, no. 1, Aug. 2016. [Online]. Available:

https://www.nature.com/articles/npjqi201629

[14] J. Heinsoo, C. K. Andersen, A. Remm, S. Krinner, T. Walter, Y. Salathé, S. Gasparinetti, J.-C. Besse, A. Potočnik, A. Wallraff, and C. Eichler, "Rapid High-fidelity Multiplexed Readout of Superconducting Qubits," *Physical Review Applied*, vol. 10, no. 3, p. 034040, Sep. 2018. [Online]. Available: https://link.aps.org/doi/10.1103/PhysRevApplied.10.034040

[15] R. Vijay, C. Macklin, D. H. Slichter, S. J. Weber, K. W. Murch, R. Naik, A. N. Korotkov, and I. Siddiqi, "Stabilizing Rabi oscillations in a superconducting qubit using quantum feedback," *Nature*, vol. 490, no. 7418, Oct. 2012. [Online]. Available: https://www.nature.com/articles/nature11505

[16] N. Ofek, A. Petrenko, R. Heeres, P. Reinhold, Z. Leghtas, B. Vlastakis, Y. Liu, L. Frunzio, S. M. Girvin, L. Jiang, M. Mirrahimi, M. H. Devoret, and R. J. Schoelkopf, "Extending the lifetime of a quantum bit with error correction in superconducting circuits," *Nature*, vol. 536, no. 7617, Aug. 2016. [Online]. Available: https://www.nature.com/articles/nature18949

[17] P. Campagne-Ibarcq, S. Jezouin, N. Cottet, P. Six, L. Bretheau, F. Mallet, A. Sarlette, P. Rouchon, and B. Huard, "Using Spontaneous Emission of a Qubit as a Resource for Feedback Control," *Physical Review Letters*, vol. 117, no. 6, p. 060502, Aug. 2016. [Online]. Available: https://link.aps.org/doi/10.1103/PhysRevLett.117.060502

[18] "Quantum Machines Website," https://www.quantum-machines.co/.

[19] "Zurich Instruments Website," https://www.zhinst.com.

[20] "Keysight Technologies Website," https://www.keysight.com.

[21] Xilinx, "Zynq UltraScale+ RFSoC," https://www.xilinx.com/products/silicon-devices/soc/rfsoc. html, 2008, [Online; accessed 22-Jan-2022].

[22] "Zcu111 evaluation board," https://www.xilinx.com/content/dam/xilinx/support/documentation/ boards_and_kits/zcu111/ug1271-zcu111-eval-bd.pdf.

[23] T. J. Rouphael, "Chapter 7 - uniform sampling of signals and automatic gain control," in *RF and Digital Signal Processing for Software-Defined Radio*, T. J. Rouphael, Ed. Burlington: Newnes, 2009, pp. 199–234. [Online]. Available: https://www.sciencedirect.com/science/article/ pii/B9780750682107000072

[24] R. Baker, *CMOS Mixed-Signal Circuit Design, Second Edition*, 12 2008.

[25] Stanford Research Systems, "SG390 Series RF Signal Generators," https://www.thinksrs.com/downloads/pdfs/manuals/SG390m.pdf, 2017, [Online; accessed 22-Jan-2022].

[26] Tektronix, "TSG4100A Series RF Signal Generators," https://download.tek.com/manual/TSG4100A-Series-RF-Signal-Generator-User-Manual-071315002.pdf, 2017, [Online; accessed 15-Feb-2022].

[27] Signal Hound, "VSG60A Vector Signal Generators," https://signalhound.com/sigdownloads/VSG60/VSG60A-Product-Manual.pdf, 2020, [Online; accessed 20-Feb-2022].

[28] Keysight Technologies, "N5166B CXG, RF Vector Signal Generator," https://www.keysight.com/in/en/assets/7018-06626/data-sheets/5992-3959.pdf, 2021, [Online; accessed 20-Feb-2022].

[29] T. Collins, R. Getz, D. pu, and A. M. Wyglinski, *Software-Defined Radio for Engineers*, 2018.

[30] A. L. Borja, J. Carbonell, V. E. Boria, J. Cascon, and D. Lippens, "A 2% Bandwidth C-Band Filter Using Cascaded Split Ring Resonators," *IEEE Antennas and Wireless Propagation Letters*, vol. 9, pp. 256–259, 2010, conference Name: IEEE Antennas and Wireless Propagation Letters. [Online]. Available: https://ieeexplore.ieee.org/stamp/stamp.jsp?tp=&arnumber=5439980

[31] Analog Devices, "HMC892ALP5E, Tunable Band-pass Filter," https://www.analog.com/en/products/hmc892a.html?doc=HMC892ALP5E.pdf#product-overview, 2018, [Online; accessed 18-Feb-2022].

[32] H. Paik, D. I. Schuster, L. S. Bishop, G. Kirchmair, G. Catelani, A. P. Sears, B. R. Johnson, M. J. Reagor, L. Frunzio, L. I. Glazman, S. M. Girvin, M. H. Devoret, and R. J. Schoelkopf, "Observation of High Coherence in Josephson Junction Qubits Measured in a Three-Dimensional Circuit QED Architecture," *Physical Review Letters*, vol. 107, no. 24, p. 240501, Dec. 2011. [Online]. Available: https://link.aps.org/doi/10.1103/PhysRevLett.107.240501